Pharm Res (2011) 28:66–81
DOI 10.1007/s11095-010-0167-x

RESEARCH PAPER

In Vivo, In Situ Imaging of Microneedle Insertion into the Skin of Human Volunteers Using Optical Coherence Tomography

Siôn A. Coulman • James C. Birchall • Aneesh Alex • Marc Pearton • Bernd Hofer • Conor O'Mahony • Wolfgang Drexler • Boris Považay

Received: 19 January 2010 / Accepted: 28 April 2010 / Published online: 13 May 2010

ABSTRACT

Purpose To gather sub-surface *in situ* images of microneedle-treated human skin, *in vivo*, using optical coherence tomography (OCT). This is the first study to utilise OCT to investigate the architectural changes that are induced in skin following microneedle application.

Methods Steel, silicon and polymer microneedle devices, with different microneedle arrangements and morphologies, were applied to two anatomical sites in human volunteers following appropriate ethical approval. A state-of-the-art ultrahigh resolution OCT imaging system operating at 800 nm wavelength and <3 μm effective axial resolution was used to visualise the microneedle-treated area during insertion and/or following removal of the device, without any tissue processing.

Results Transverse images of a microneedle device, *in situ*, were captured by the OCT system and suggest that the stratified skin tissue is compressed during microneedle application. Following removal of the device, the created microchannels collapse within the *in vivo* environment and, therefore, for all studied devices, microconduit dimensions are markedly smaller than the microneedle dimensions.

Conclusions Microchannels created in the upper skin layers by microneedles are less invasive than previous histology predicts. OCT has the potential to play a highly influential role in the future development of microneedle devices and other transdermal delivery systems.

KEY WORDS *in vivo* · microneedle · optical coherence tomography · skin · transdermal

ABBREVIATIONS

OCT Optical coherence tomography

INTRODUCTION

Topical application of medicinal formulations, e.g. creams, ointments and transdermal patches, is a non-invasive and patient-friendly method of drug delivery. However the barrier properties of the outermost skin layer, the stratum corneum, significantly restrict the number of drug candidates that can be delivered via this route. Traditional transdermal delivery systems are therefore restricted to a small number of drug candidates with specific physiochemical properties, i.e. high potency, low molecular weight (<500 Daltons) and moderate lipophilicity (1). In the last decade, there has been a concerted effort from academic and industrial scientists to produce a delivery system that can facilitate transdermal penetration of a more diverse range of therapeutic candidates, including biological

Electronic supplementary material The online version of this article (doi:10.1007/s11095-010-0167-x) contains supplementary material, which is available to authorized users.

S. A. Coulman (✉) · J. C. Birchall · M. Pearton
Gene Delivery Research Group, Welsh School of Pharmacy
Cardiff University
Cardiff CF10 3NB, UK
e-mail: coulmansa@cardiff.ac.uk

B. Hofer · W. Drexler · B. Považay
Center of Medical Physics and Biomedical Engineering
Medical University Vienna
Vienna 1090, Austria

A. Alex · B. Hofer · W. Drexler · B. Považay
School of Optometry and Vision Sciences, Cardiff University
Cardiff CF24 4LU, UK

C. O'Mahony
Tyndall National Institute, University College Cork, Lee Maltings
Cork, Ireland

macromolecules. Such a feat could revolutionise drug delivery to and through the skin.

One proposed strategy to overcome the skin barrier is to create conduits, with micron dimensions, within the epidermal layer either by localised tissue ablation (thermal ablation (2,3), radiofrequency ablation (4,5)) or mechanical penetration (microneedle devices (6)). Interestingly, the latter of these technologies, the microneedle device, was conceptualised in the 1970s (7). However, it was the advent of silicon microfabrication methods, developed for the microelectronics industry, which enabled manufacture of the first microneedle device (8). In the last decade, engineering capabilities have developed significantly, and the microneedle device has now been manufactured using a range of materials and in a variety of geometries (9–11).

Laboratory studies have successfully used microneedle devices to create micron-sized channels within skin. Importantly, the created conduits are able to facilitate localised delivery of a range of therapeutic candidates, including small drug molecules (12), peptides (13,14), proteins (15–20), nanoparticles (9,21) and plasmid DNA (22). Within such studies, the depth and morphology of microchannels, which are created in the tissue upon removal of the device, are typically characterised by traditional histological methods. These features provide the researcher with an indication of the dimensions of microneedle-induced conduits and the invasiveness of specific microneedle designs, and thus these studies are relevant to drug delivery and device safety.

To date, the majority of microneedle studies have been conducted using animal models, and, although these models provide essential pre-clinical data, there are significant architectural and immunological differences between human and animal skin (23). Therefore, microneedle channels created in animal skin are not an accurate representation of the human environment. *Ex vivo* human skin provides an anatomically relevant model for microneedle studies (24). However, excision of the skin from its natural environment results in considerable biomechanical changes to the tissue. These changes must be considered when interpreting evidence of microneedle penetration.

In recent years there have been an increasing number of studies that have examined microneedle penetration in human volunteers (25–29). This provides data that can often be directly extrapolated to the clinical environment. The principal goal of these studies has been to evaluate the pain associated with microneedle insertion. As a corollary, microneedle penetration is often assessed by application of a staining agent to permit *en face* visualisation of microchannels (26,29). Trans-epidermal water loss (TEWL) can also provide a surrogate measure of *in vivo* microneedle-mediated tissue disruption (25–27); however, this laboratory technique suffers from a number of limitations, and the quality of the data achieved is variable (30). Transverse imaging of microchannel structure relies upon biopsy of the microneedle-treated skin area and subsequent histological analysis, i.e. fixation and sectioning. These experimental procedures inevitably alter the skin structure and produce artefacts. Limitations in analytical tools and procedures have therefore prevented the accurate elucidation of microconduit structure in human skin, *in vivo*, following application of a microneedle or similar minimally invasive device.

Significant advances have been made in optical imaging methods over the previous decade. At the forefront of these techniques is optical coherence tomography (OCT). OCT is a non-invasive interferometric technique that is capable of resolving skin architecture, *in vivo* and in real time, at micrometer scale and up to a depth of 1–2 mm, solely based on local optical backscatter (31,32). The principles of OCT are often likened to ultrasound, and the technology has been used to characterise structural and biomechanical features of both 'normal' and diseased human skin (33–39). Whilst OCT is establishing itself as a routine imaging method in ophthalmology, the evaluation of skin is at a more developmental stage. Continuous advancements of light source and detection system technology have lead to improvements in speed, resolution, sensitivity, penetration depth and contrast necessary for histology quality imaging in dermatology (40). Investigation of skin disruption in human subjects, following treatment with novel intra-/trans-dermal drug delivery systems, has not been reported due to the limited image quality and resolution of earlier OCT systems. Interestingly, microneedle devices have been used in some animal studies to deliver agents across the epidermal layer, with the goal of enhancing specific OCT imaging parameters (41–43). However, these studies do not characterise microneedle penetration due to the limited resolution of the OCT imaging systems that were used.

The aim of this investigation is to use a state-of-the-art OCT system, *in vivo*, to obtain *in situ* images of microneedle-treated human skin. This will provide unique information on the morphological changes that are induced following microneedle application to the skin surface. Further, this study will provide evidence to support the fundamental concept of the microneedle device as a minimally invasive means to overcome the outer skin barrier and is the first comprehensive investigation of the potential of current OCT imaging systems in microneedle research.

MATERIALS AND METHODS

Microneedle Devices

Two of these devices were manufactured by laser-cutting stainless steel sheets using a process described previously

Table I A Summary of the Characteristics of the Devices Used in This Study

ID	Device name	Microneedle characteristics				
		Population	Order	Length	Material	Surface finish
A	In-plane steel	5	Row	700 μm	Steel	electropolished
B	Out-of-plane steel	50	5 × 10	700 μm	Steel	electropolished
C	Silicon array	16	4 × 4	280 μm	Silicon	platinum coated
D	Polymer array	13	Concentric circles	Outer - 600 μm Inner - 400 μm	Polymer	polycarbonate
E	Hypodermic 26G	1	–	10,000 μm	Steel	polished

(44). Within this manuscript, these will be referred to as (A) in-plane steel microneedles, which consist of a row of five adjacent microneedles, and (B) out-of-plane steel microneedles, arranged in an array of 50 microneedles that protrude orthogonally from a steel sheet. The third microneedle device (C) was fabricated and supplied by Tyndall National Institute and consists of an array of silicon microneedles that have been produced using wet-etching technology (45). The final microneedle device (D) was a prototype polycarbonate polymer array, produced at Cardiff University, using an injection moulding process. A 26 gauge hypodermic needle (E), used in clinical practice for intradermal injections, was used as a comparative delivery device. Steel microneedles (A & B) can be directly manipulated by the user. However silicon and polymer arrays were mounted upon applicator devices, a practical necessity owing to their smaller dimensions. Table I provides a summary of the characteristics of the devices used in this study.

SEM Analysis of Microneedle Devices

All microneedles were inspected prior to, and following, application to the skin to ensure that the integrity of the device was maintained. Steel microneedle devices, the hypodermic needle and the silicon array were mounted on an aluminium stub and examined using a Philips XL-20 Scanning Electron Microscope (Philips, Eindhoven, The Netherlands). Polymer microneedles were gold sputter-coated (EM Scope, Kent, UK) prior to SEM analysis.

Optical Coherence Tomography System

Imaging was performed using a hand-held probe that was connected to the spectrometer-based frequency-domain OCT device via an optical fibre link (Fig. 1), operating at 20,000 depth scans per second. It reached an axial resolution of <3 μm in tissue by using a broadband laser light source (Ti:sapphire) that illuminated the tissue with less than 1 mW at 800 nm central wavelength and 160 nm bandwidth (46). The 1 Gigavoxel cube (1024 × 1024 × 1024 voxel) was acquired in ~50 s and was sampled using parameters approaching critical sampling, approximately 5 μm transversally at an approximately 10 μm transversal resolution, across a field of view of typically 9 × 9 mm and 3 mm sampling depth. The depth of field, where the image is still well focussed, could be specified as ~600 μm; hence, the focus was typically set at the papillary dermis. Despite the availability of the more penetrative broadband 1,060 nm and 1,300 nm lasers, the 800 nm wavelength

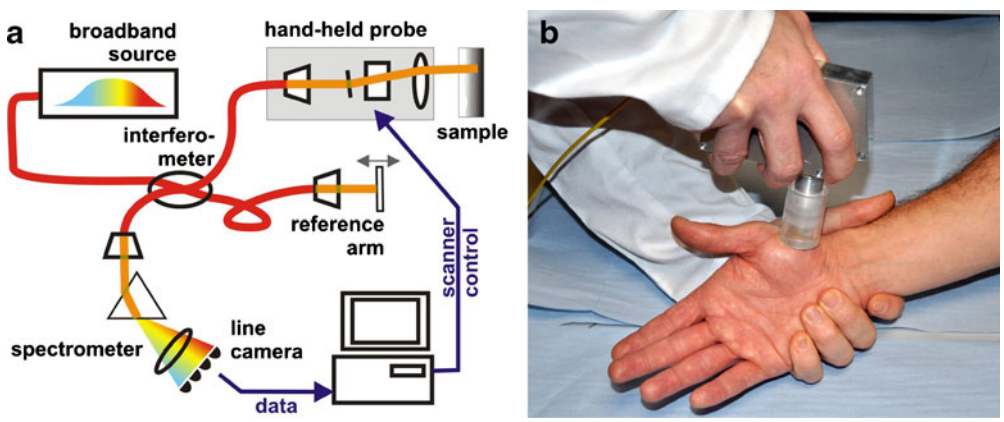

Fig. 1 (**a**) Schematic representation of OCT and (**b**) the handheld probe used to capture images in human subjects.

region provided greater axial resolution and contrast whilst maintaining sufficient penetration depth, and therefore was selected for this study.

Study Design

Approval for the application of microneedle devices to human subjects was obtained from a Cardiff University ethics committee; research followed the tenets of the Declaration of Helsinki. Human volunteers were recruited from the staff population at the Welsh School of Pharmacy, Cardiff University, and participants were provided with an information sheet and consent form prior to the study. Three healthy Caucasian male volunteers, aged between 21 and 40 years of age with no pre-existing skin conditions, were chosen and randomly allocated to microneedle treatments. Participant One was treated with steel microneedles (in-plane and out-of-plane), Participant Two with the silicon microneedles and Participant Three with polymer microneedles. Additionally, participants were also treated with a 26-gauge needle, inserted into the skin at an angle of approximately 15°, to represent the traditional intradermal injection process (positive control).

Two anatomical sites were selected for microneedle treatment, the upper arm and the palm. The microneedle device is currently being investigated as a means of facilitating intradermal vaccination (18,19,28,47), and the upper arm, a recognised intradermal vaccination site (48), was therefore selected as an easily accessible and clinically relevant anatomical site. At the palmar site the skin possesses a low-scattering, thickened stratum corneum which is interspersed by a dense regular arrangement of highly scattering sweat ducts. The palmar site was therefore selected for its optical properties and provided the greatest possibility of microneedle channel detection using OCT imaging. Additionally, the hand is one of the most likely sites of needle-stick injury, and therefore evaluation of microneedle penetration at this site would inform safety aspects of microneedle systems.

Experimental Protocol

The study took place in Cardiff School of Optometry and Vision Sciences. Following receipt of written consent, a proposed treatment area (2 cm^2) on the left hand of the volunteer was identified, swabbed with ethanol and marked on the border of the imaging region to ensure that repeat images of the treatment site could be obtained. A handheld probe (Fig. 1b) was then positioned on the site, and parameters of the OCT system were optimised by the operator using the real-time preview. To avoid the strong reflections from an air interface, a thin film of index matching fluid (i.e. glycerine or a commercial water-based gel) was applied to a flat tilted cover glass, which was mounted in front of the telecentric ~30 mm diameter objective of the handheld probe. The gel therefore acted as a contact medium. Fixation was achieved simply by resting the probe on the body of the subject and was secured by the hands of the operator. During alignment and measurement, the imaging volume was controlled by the real-time view of the local cross-section.

Following image capture, the probe was removed, and the selected area was cleaned, swabbed and treated with the microneedle device. Microneedle administration involved downward application of a sterilised microneedle device to the skin surface at a sufficient pressure to enable skin penetration. All devices were held in place for 5 s and subsequently withdrawn. Index matching fluid was then applied topically to the microneedle-treated area, which was imaged using the hand-held probe, as described previously. The same procedure was used to examine treatment with a sterile 26G hypodermic needle at an adjacent area (positive control). Additionally, the two-dimensional nature of the in-plane steel microneedle array also permitted OCT imaging of the skin with the microneedle device *in situ*. This was performed by tilting the array upon insertion, holding the array in position with a forceps and subsequently applying the hand-held probe above the microneedle-treated area. To accommodate the greater working distance the objective was refocused.

Following application, the microneedle devices were immersed in 70% ethanol for at least 24 h prior to their visual analysis by SEM. Volunteers remained in the treatment room for at least 15 min following application of the devices to ensure there were no localised adverse effects. The experimental protocol was then repeated for the upper arm region.

Optical Coherence Tomography Image Analysis

After acquisition with Labview (National Instruments), the data was stored to a high-speed RAID array and converted from its original format to its three-dimensional representation using specifically designed routines in Matlab (Mathworks) and ImageJ (U. S. National Institutes of Health). The first stage was correction of the spectral data for non-linearities, dispersive shifts and unwanted background signals followed by conversion from its spectral form, by Fourier-transformation, into a sequence of slices. Slices were then transversally rearranged to eliminate motion artefacts, and the tilt was numerically compensated. The densely sampled three-dimensional stack containing 16-bit data was filtered to reduce noise and speckle by non-linear filtering of outliers and local convolution. Cross-sections and *en face* scans were generated by local integration in depth across selected sites and successive adjustment of the

contrast and brightness values. *En face* images of the skin do not represent the tissue-air interface but are obtained at a sub-surface depth within the tissue, as indicated in the accompanying figures.

RESULTS

SEM Analysis of Microneedle Devices

Scanning electron micrographs of each microneedle device are captured alongside the 26G needle, illustrating the considerable difference in the dimensions, shapes, materials and arrangements of these penetrative devices (Fig. 2).

In Vivo Analysis of Device Penetration Using OCT

The OCT system gathers real-time data as a sequence of images in the x-z plane (with x and y as transversal coordinates and z as the depth direction) and therefore can produce 2D and 3D images of biological tissue. For clarity, data are predominantly presented as 2D images of (1) sub-surface *en face* representations of the skin and (2) transverse or tomographic cross-sections, perpendicular to the skin surface. A video (available in Electronic Supplementary Material online) consists of a sequence of transverse slices and therefore provides further anatomical information and an opportunity to view associated morphological structures in the untreated and treated regions.

Hypodermic Needle Insertion into the Palmar Region

Fig. 3 contains two typical slices gathered by the OCT imaging system (Fig. 3d and e). Before analyzing the area of interest, it is important to recognise the regular morphological features of human palmar skin, which are illustrated on the right side of Fig. 3d. The superficial dermatoglyphics of the skin surface and a characteristic thickened stratum corneum are easily discernible. This layer measures approximately 200 μm in depth and appears as a homogenous dark-grey band, separated from the viable epidermis by a thin, distinctively darker contour. Characteristic spiralling structures of eccrine sweat ducts are also observed in the stratum corneum of the palmar skin (Fig. 3d). The highly scattering band of the underlying epidermis appears as two layers (stratum granulosum and stratum spinosum) that are well separated by the thin low scattering region of the stratum lucidum, found in the thicker palmar skin only. However, the dermo-epidermal junction zone is less well defined by the OCT image. The remainder of the skin

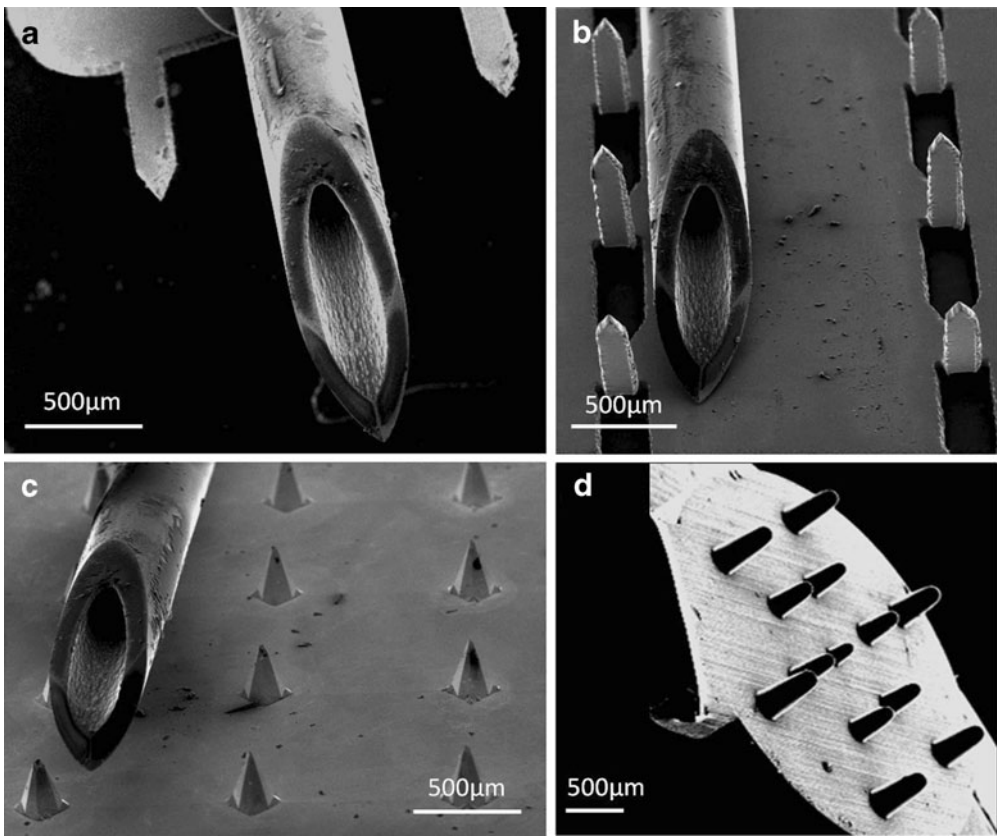

Fig. 2 Scanning electron micrographs of (**a**) in-plane steel, (**b**) out-of-plane steel, (**c**) silicon array and (**d**) polymer array, microneedle devices. The tip of a 26G hypodermic needle, used in these studies, has been included in images (**a**)–(**c**).

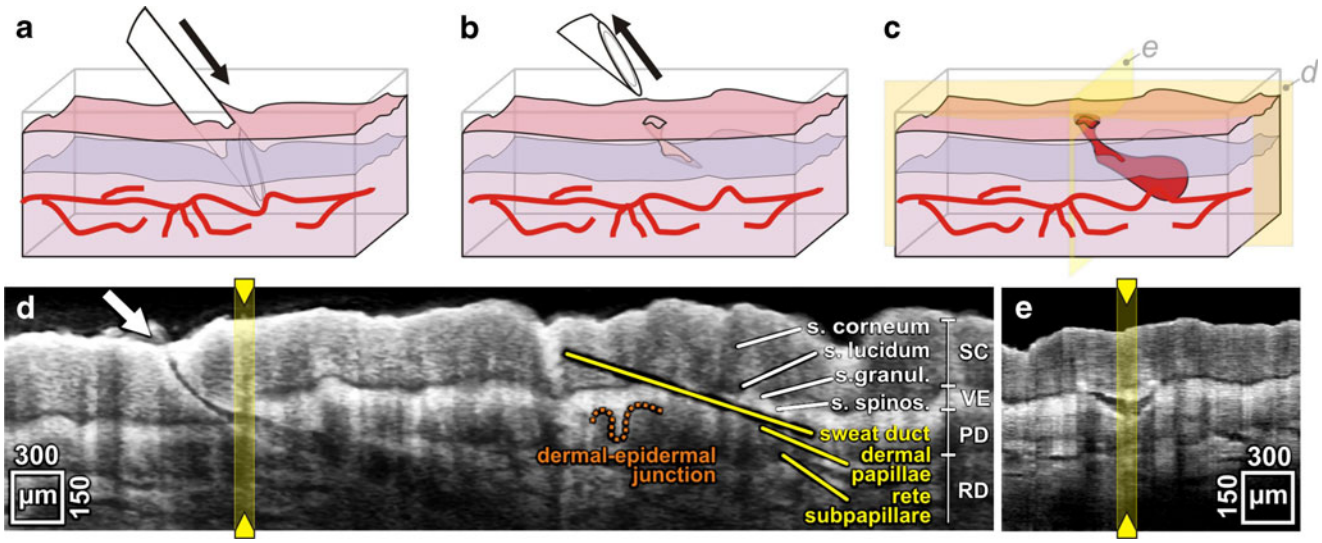

Fig. 3 Schematic images (**a**) to (**c**) illustrate the experimental process used to obtain the OCT images pictured in (**d**) and (**e**). Figs. (**a**) and (**b**) depict needle insertion and removal, and Fig. (**c**) provides a reference to the location of OCT scans, depicted in (**d**) and (**e**), within the tissue volume. The *yellow line* in image (**d**) indicates the position of the accompanying perpendicular OCT slice (**e**), and vice-versa, extracted from the volume. The stratified architecture of skin tissue is highlighted in (**d**) with epidermis delineated into the stratum corneum (SC) and the viable epidermis (VE). The dermal-epidermal junction sits above the papillary dermis (PD), which in turn overlies the strongly vascularised reticular dermis (RD). A *dashed orange line* highlights the border between the epidermal and dermal layers. The *white arrow* in 3d indicates the position of hypodermic needle insertion.

section, the reticular dermis, is demarcated from the papillary dermis by a signal-poor strip, corresponding to the rete subpapillare. This appears as a heterogeneous layer containing darkened, elongated, horizontal, signal-free areas, which correspond to dermal blood vessels.

Insertion of a hypodermic needle caused significant changes to the 'normal' tissue morphology (video available in Electronic Supplementary Material online). The two cross-sectional images (Fig. 3d and e), analysed at 90° to each other, exemplify the tissue disruption caused by the intradermal injection process. A collapsed channel, left by the hypodermic needle immediately following removal from the skin, follows the path of the needle into the vascularised reticular dermis (Fig. 3d). Needle-induced disruption of blood vessels in this region has inevitably resulted in localised bleeding and the subsequent extrusion of blood into the tens-of-microns-wide channel that has been fashioned by the needle. Notably, the diameter of the needle channel is significantly reduced in the stratum corneum region (10–20 µm) compared with the viable epidermis (>40 µm). Expansion of this channel continues into the papillary dermis, and a diffuse darkened area of blood can be visualised in the reticular dermis.

A perpendicular slice of this microchannel, at the stratum corneum/epidermal border, provides an alternate view of needle penetration (Fig. 3e). A dark v-shaped region, over 300 µm in width, illustrates the architectural damage created in the tissue during insertion and retraction of the needle. This is caused by the bevelled tip of the hypodermic needle. A sequence of perpendicular slices can be viewed in succession, in the direction of needle penetration, to visualise needle-induced tissue damage and the resulting morphological changes in disparate layers of the tissue (video available in Electronic Supplementary Material online).

Hypodermic Needle Insertion into the Upper Arm

An *en face* image of the skin, taken at a superficial level of the epidermis in the upper arm, reveals recognisable inherent structural features including hairs and the characteristic pavement pattern of the skin dermatoglyphics (Fig. 4a). The darkened central area is a result of bleeding in the interstitial space of dermal tissue, caused by insertion and subsequent removal of the hypodermic needle (Fig. 4a). The sub-surface structure of skin in the upper arm (Fig. 4b–d) differs significantly from the thicker skin of the palmar region. In this anatomical region the stratum corneum is thinner, existing as a less than 20 µm thin bright region. The underlying viable epidermis is a well-defined homogenous highly scattering layer with a depth of 80–90 µm. Below this is the poorly defined dermal layer, containing a network of identifiable blood vessels.

Transverse images of the tissue at the point of needle insertion reveal a similar structure to that identified in the palmar region (Fig. 4c). However, there are notable differences in the shape of the microchannel created in the upper arm, attributable to the contrasting tissue architectures. Additionally, perforation of a blood vessel(s) has resulted in a localised haematoma and significant swelling of the dermal tissue, visible as an elevation in the

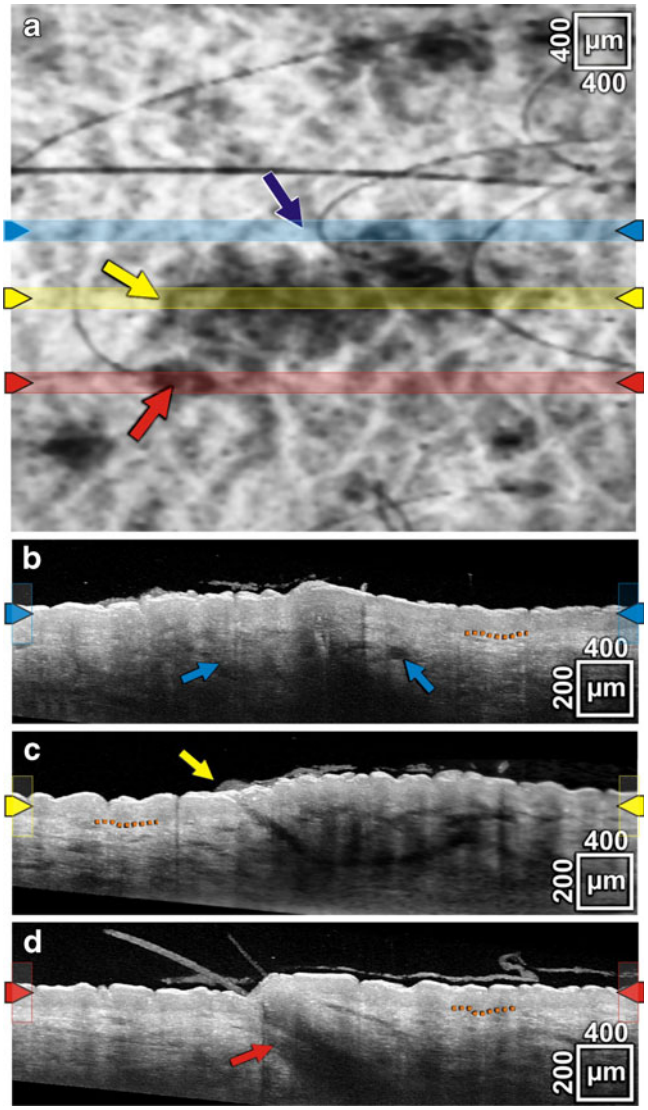

Fig. 4 OCT images of human skin, in the upper arm region, treated with a 26G hypodermic needle. The *en face* image in (**a**) is obtained by OCT analysis of the treated skin tissue at a sub-surface location within the viable epidermis (indicated by the complementary *colours arrows* at the edges of images (**b**)–(**d**)). The blue line in the *en face* image (**a**) highlights the position of the OCT slice pictured in (**b**), whilst the yellow line refers to image (**c**) and the red line to image (**d**). The blue arrow in image (**b**) demonstrates the sub-surface appearance of the created haematoma. Image (**c**) depicts the channel created by the hypodermic needle, the *yellow arrow* indicating the direction of needle insertion. The hair follicle pictured in image (**d**) provides a useful anatomical reference. The *red arrow* points towards a structure possibly associated with the arrector muscle of the hair follicle. *White arrows* on the border of the transverse images provide the sub-surface location of the *en face* image and the integration depth (**a**). A *dashed orange line* in (**b**–**d**) highlights the border between the epidermal and dermal layers.

cross-sectional image (Fig. 4c). A diffuse area of blood is also present in adjacent cross-sections, demonstrating the extent of the haematoma (Fig. 4b). A transverse image of a hair follicle (Fig. 4d) provides reference to an intrinsic skin structure, which possesses comparable dimensions to the channel created by the hypodermic needle.

In-Plane Steel Microneedle Insertion into the Palm and Upper Arm

In situ images capture penetration of the in-plane microneedle device into human palmar skin (Fig. 5). Interestingly, this figure highlights the deformation of palmar skin upon microneedle insertion and indicates that the skin compresses below the point of individual needle insertion in all but the outermost needle (Fig. 5d). The biomechanical properties of the skin therefore resist microneedle penetration, and thus microneedle insertion is incomplete. Removal of the microneedle device results in the creation of discrete darkened areas, arranged in an ordered pattern that mirrors the spacing of microneedles in the in-plane device (Fig. 6 and video available in Electronic Supplementary Material online). A dense population of eccrine sweat glands, visualised as discrete non-pigmented regions of approximately 100 µm in diameter, are also apparent and provide a useful anatomical reference for the magnitude of microneedle disruptions (Fig. 6b). Transverse sections indicate that the 700 µm-long in-plane steel microneedles create microchannels in palmar skin, up to 300 µm in depth, that appear to be primarily limited to the stratum corneum (Fig. 6c). However, an area of tissue disruption at the stratum corneum/viable epidermis border, on the right of Fig. 6c (yellow arrow) indicates that microneedles may also penetrate to greater depths under some circumstances (i.e. at the end of the array, where the tissue lacks compression by the needle-mount).

En face images of skin in the upper arm region, treated with the in-plane microneedle device, are comparable to those visualised at the palmar site (Fig. 7a). Microneedle channels can be visualised, *en face*, as equally spaced darkened regions in the epidermal layer (Fig. 7a), and transverse images enable the morphology of these tissue disruptions to be determined (Fig. 7b and c). Images suggest that the microneedle device penetrated to a depth of less than 100 µm, resulting in tissue disruption that is largely confined to the upper epidermal layer. In fact, microneedle devices seem to induce tissue disruption rather than distinctive microconduits, and these can be difficult to differentiate from the inherent dermatoglyphics of the skin (Fig. 7c). Therefore, the 3D imaging capabilities of OCT assist identification and the subsequent analysis of microneedle-induced skin disruptions, *in vivo*. For invasive devices, such as the hypodermic needle, blood acts as a contrasting agent for OCT imaging and therefore aids identification of the tissue disruption (Fig. 3d and e). However, the absence of bleeding in microneedle-treated skin, combined with the reduced dimensions of the created microdisruptions, results in a less distinctive microchannel appearance.

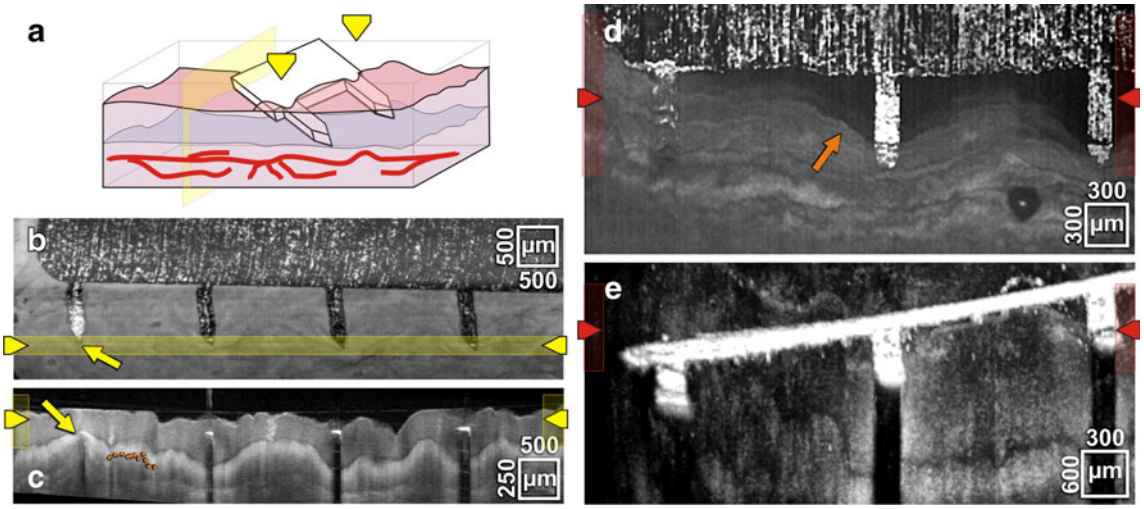

Fig. 5 OCT schematic image (**a**) portrays the experimental procedure used to capture the OCT images in this figure. Images (**b**)–(**e**) were obtained whilst the in-plane steel microneedle device was *in situ*. *Yellow arrows* in (**b**) and (**c**) are used to highlight corresponding areas at the microneedle tip. The *orange arrow* in (**d**) highlights the deformation of the tissue, which limits the microneedle penetration. Image (**e**) is an orthogonal projection to (**d**), as indicated by the range indicators. Images (**d**) and (**e**) are generated from multiple slices using an algorithm referred to as the maximum intensity projection. A *dashed orange line* in (**c**) highlights the border between the epidermal and dermal layers.

Out-of-Plane Steel Microneedle Insertion into the Palm and Upper Arm

Treatment of human skin using the array of 50 blade-like steel microneedles produced comparable results to that of the in-plane microneedles, in both the palmar and upper arm regions (Figs. 8 and 9). The pattern of microdisruptions created in the stratum corneum of palmar skin, by the steel microneedle device, closely resembles the geometric arrangement of individual microneedles within an array (Fig. 8a). Re-slice of the data to produce transverse images indicates that the tissue is deflected downwards, immediately after microneedle treatment, below each point of microneedle penetration (Fig. 8b). However, identification of a definitive conduit is disguised by shadowing, a recognised artefact in the OCT imaging process. This artefact is caused by microneedle-induced physical disruption of the upper skin layers and the inevitable creation of an air-filled cavity at the skin surface. Although this hampers imaging of microconduits, it provides a useful practical marker for the detection of microchannels within the tissue. Reflective effects were present, but less evident, in previous images of microneedle-treated skin (e.g. Figs. 5c, 6c and 7c). In hypodermic-treated skin (Figs. 3d, e and 4a–d), the presence of blood, acting as a contrast agent, in the conduit prevented this artefact. It should also be noted that the square distribution of the out-of-plane needle array results in shallower penetration of the individual needles compared to the in-plane row of needles. Although there was also some evidence of microneedle-induced microchannels in the upper arm region (Fig. 9a and b), detection was difficult in the thinner skin tissue.

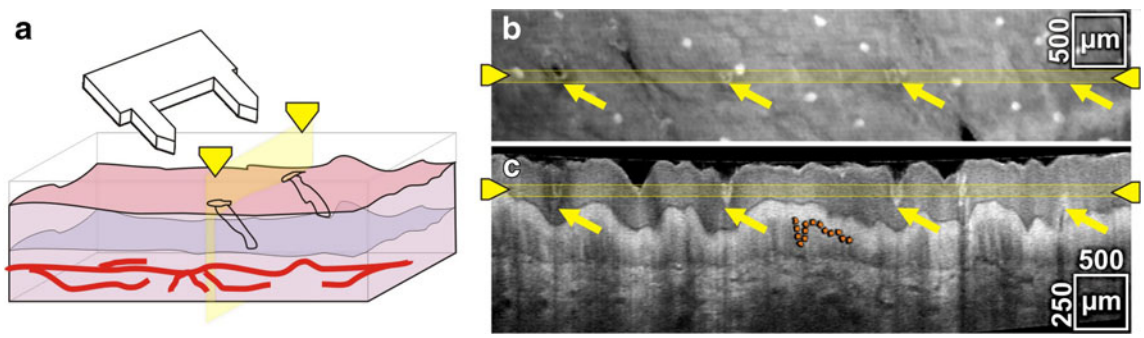

Fig. 6 The schematic image (**a**) portrays the experimental procedure use to capture transverse OCT images of the palmar skin following removal of in-plane steel microneedles. The *en face* image in (**b**) is obtained by OCT analysis of the skin tissue at a sub-surface location within the thickened stratum corneum layer (indicated by the location of the *yellow line* in (**c**)). Image (**c**) provides a cross-sectional view of the microneedle-treated area of tissue. *Yellow arrows* in (**b**) and (**c**) identify microdisruptions in the skin tissue. A *dashed orange line* in (**c**) highlights the border between the epidermal and dermal layers.

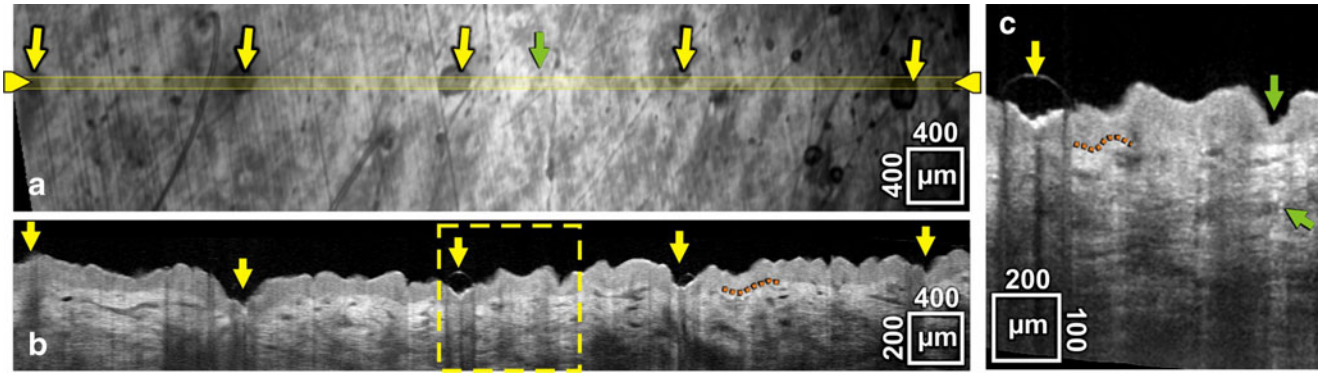

Fig. 7 OCT images of human skin, at the upper arm site, treated with an in-plane steel microneedle array. The *en face* image in (**a**) is obtained by OCT analysis of the skin tissue at a sub-surface location within the epidermal layer. The *dashed rectangle* in (**b**) is used to indicate the portion of the OCT section that has been magnified in (**c**). *Yellow arrows* highlight the location of microneedle-induced microdisruptions. A *green arrow* is used to identify an adjacent sweat duct. A *dashed orange line* in (**b**) and (**c**) highlights the border between the epidermal and dermal layers.

Silicon Array Insertion into the Palmar and Upper Arm Region

Microneedle-induced disruption of the skin was less obvious following treatment with the pyramidal silicon microneedle array. Meticulous analysis of OCT images revealed only minor architectural changes in the upper layers of the skin, at both treatment sites (Figs. 10 and 11). Microchannels are therefore restricted to the superficial skin layers, and images suggest that the skin structure recovers following insult with these smaller microneedles. The distinctive spiralling structures of the eccrine sweat ducts, captured in both the palmar and upper arm regions (see green arrows on Fig. 10c and d), provide anatomical reference for the dimensions of the created microdisruptions. Glycerine was used to promote optical clearing, but channels only appeared to extend into the lower layers of the stratum corneum in the thicker palmar skin (Fig. 10a and b). The cross-section of Fig. 10b is slightly slanted *versus* the sequence of perforations and thus gives some insight into the three-dimensional crater-like structure of the compres-

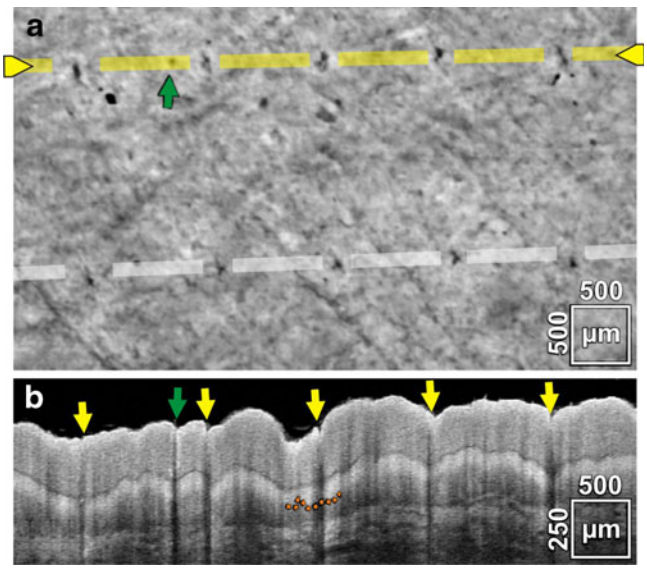

Fig. 8 OCT images of human palmar skin, treated with an out-of-plane steel microneedle array. The *en face* image in (**a**) is obtained by OCT analysis of the skin tissue at a sub-surface location within the stratum corneum layer. *Dashed lines* highlight the array pattern of microdisruptions in the tissue, with gaps between the lines highlighting areas of microneedle penetration. A cross-section (**b**) has been produced along the *dashed yellow line*. *Yellow arrows* in (**b**) highlight the location of microdisruptions in the skin surface. An opening of similar size is formed at the surface of a sweat duct, which is indicated by the *green arrows*. A *dashed orange line* in (**b**) highlights the border between the epidermal and dermal layers.

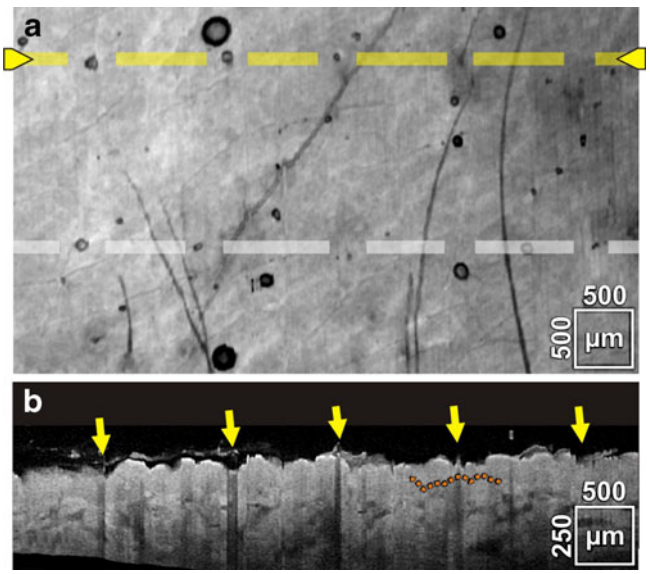

Fig. 9 OCT images of human skin of the upper arm, treated with an out-of-plane steel microneedle array. The *en face* image in (**a**) is obtained by OCT analysis of the skin tissue at a sub-surface location within the epidermal layer. *Dashed lines* highlight the array pattern of microdisruptions in the tissue, with gaps between the lines highlighting areas of microneedle penetration. A cross-section (**b**) has been produced along the *dashed yellow line*. Arrows in (**b**) highlight the location of microdisruptions in the skin surface. A *dashed orange line* in (**b**) highlights the border between the epidermal and dermal layers.

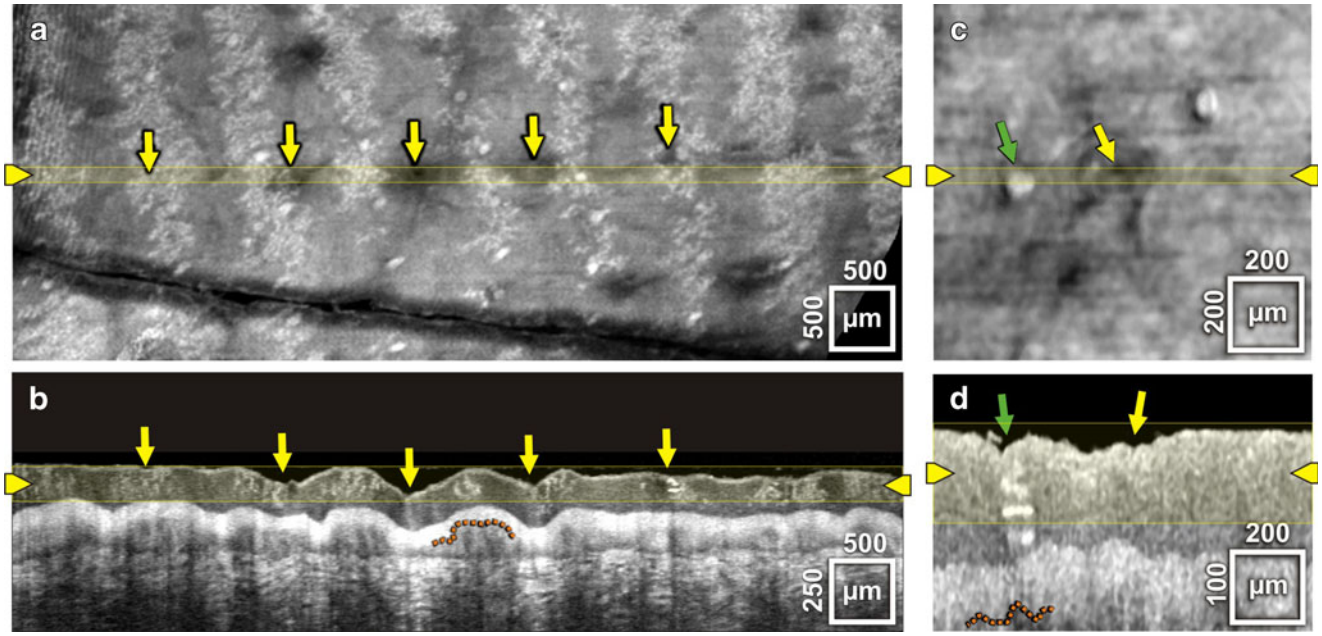

Fig. 10 OCT images of palmar human skin, treated with the silicon microneedle array using glycerine as index matching liquid that partially cleared the stratum corneum optically. The *en face* images in (**a**) and (**c**) are obtained by integration of the OCT signal within the stratum corneum layer as indicated in the corresponding cross-sections. Cross-sections, (**b**) and (**d**), have been selected at the location of the yellow indicators in *en face* images. *Yellow arrows* highlight the location of microdisruptions in the tissue, and *green arrows* identify an eccrine sweat duct. A *dashed orange line* in (**b**) and (**d**) highlights the border between the epidermal and dermal layers.

sion sites. In the thinner upper arm skin, the impressions are difficult to visualise *en face* (Fig. 11a and b) but become more obvious in the cross-section (Fig. 11c, yellow arrow), where they are comparable in size and shape to the exit region of sweat ducts.

Polymer Array Insertion into the Palmar and Upper Arm Region

Application of the prototype polymer microneedle array to the palmar region of human skin provided little conclusive evidence of microneedle penetration (Fig. 12a). Fig. 12c indicates that conduits have been created by the polymer pillars (yellow arrow) with a greater depth than those induced by the silicon pyramidal microneedles, owing to their greater length. However, the polymer array also compresses the region of tissue at the periphery of the array (Fig. 12b, blue arrows). Treatment of the upper arm region induced two concentric circles of surface disruptions, which reflect the arrangement and dimensions of microneedles within the polymer array (Fig. 13a and c). A transverse image, created by obtaining a slice across the central portion of the treated area, reveals uniformly spaced, micron-sized disruptions in the skin surface which again cause noticeable reflection artefacts, i.e. shadow-like vertical lines, visible due to the strong inclination of the surface or caused by microbubbles on the surface (Fig. 13b). These disruptions are visible as darkened areas in the superficial (Fig. 13a) and also the deeper regions (Fig. 13c) of the tissue. The edge of the circular polymer array also leaves a characteristic impression, visible as a darker portion in the

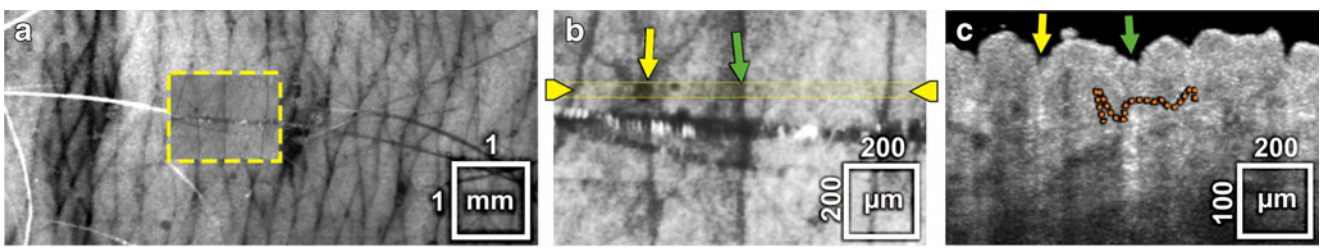

Fig. 11 OCT images of human skin of the upper arm, treated with the silicon microneedle array. *En face* images (**a**) and (**b**) are obtained by OCT analysis of the skin tissue at a sub-surface level within the epidermal layer. A cross-section (**c**) has been produced at the location of the *yellow line* in (**b**). *Yellow arrows* highlight a possible microneedle-induced microdisruption, and the *green arrow* highlights an adjacent dermatoglyphic structure. A *dashed orange line* in (**c**) highlights the border between the epidermal and dermal layers.

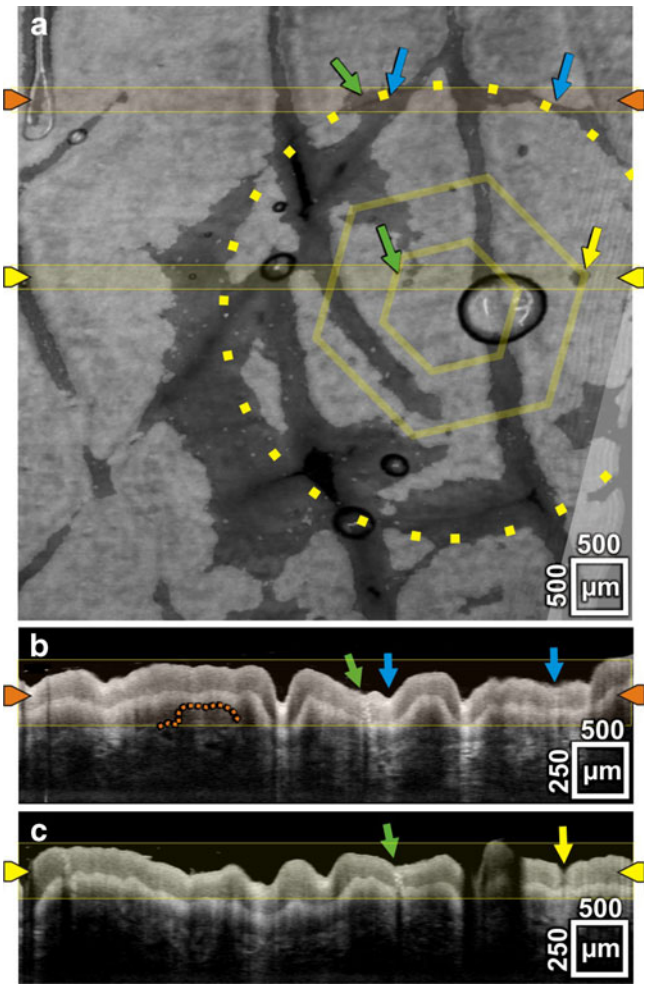

Fig. 12 OCT images of palmar human skin treated with the polymer microneedle array. The *en face* image in (**a**) is obtained by OCT analysis of the skin tissue at a sub-surface location within the stratum corneum layer as indicated by the *yellow and red arrows* in (**b**) and (**c**). The *yellow circular dotted line* highlights the impression left by the edge of the polymer array, and the hexagonal structures provide a guide to the location of microneedles, which would be positioned close to the vertices. Images (**b**) and (**c**) are OCT slices at the two locations indicated in (**a**) by the *yellow* and *red* indicators, respectively. *Blue arrows* indicate the impression by the polymer edge, *yellow arrows* highlight possible microneedle-induced micro-disruptions in the tissue, and the *green arrows* identify eccrine sweat ducts. A *dashed orange line* in (**b**) highlights the border between the epidermal and dermal layers.

superficial *en face* image (Fig. 13a) and as brightened regions, due to the shift of the highly scattering viable dermis, at a deeper position in the tissue (Fig. 13c). This feature is indicative of tissue compression. Although microchannels created by this device appear to be less than 100 µm deep, transverse images confirm breach of the skin surface at the upper arm site by the microprojections and not simply indentation of the tissue. Interestingly, images also indicate that the longer microneedles, located on the peripheral circle of the array, create disruptions that are approximately twice as deep (Fig. 13b).

DISCUSSION

The physical response of human skin to injury is dictated by the biomechanical properties of the tissue. It is difficult to reproduce these properties within laboratory models; therefore, although the number of human subjects used in this study is very small ($N=3$), the data collected provides a unique insight into the penetration performance of microneedle devices *in vivo*. This study has used an OCT imaging system to successfully capture sub-surface *in situ* images of microneedle-treated human skin and has demonstrated differences in penetration efficacy and depths using different microneedle devices. This technique could have major implications for the microneedle research community, providing unique data relating to the mechanical response of human skin to microneedle insertion and demonstrating the effect of microneedle design on penetration characteristics.

Intradermal administration of a hypodermic needle was used as a clinically relevant comparator to the microneedle device. OCT images of palmar skin, punctured by a 26G needle, indicate that the diameter of the microchannel that is created in the thickened SC layer (10–20 µm) is almost fifty times smaller than the width of the needle itself (450 µm) (Fig. 3d). This demonstrates the elasticity of the skin and the ability of the physical 'brick-and-mortar' structure of the stratum corneum to constrict following insult, an inherent physiological function of this protective external barrier. The underlying viable epidermis does not share the same biomechanical properties; therefore, as the microchannel extends into the cellular region, it becomes significantly wider. Further, perpendicular transverse images at the point of insertion suggest that removal of the needle results in displacement of a region of the tissue, leaving a distinctive v-shaped void in the centre of the viable epidermis (Fig. 3e and Electronic Supplementary Material online video). Tissue damage in the stratum corneum appears less extensive, again indicating that the compact keratin-filled layer endeavours to 'seal' following insult.

Insertion of the hypodermic needle into the upper arm resulted in the creation of a more homogenous and wider channel. Acknowledged distinctions in the tissue architecture and biomechanics at the two anatomical treatment sites, most notably the significant disparity between the thicknesses of the stratum corneum layers, contribute to the different tissue responses. This disparity might also be expected to influence microneedle penetration. However, the minimal damage caused by microneedle devices, due to the elastic properties of the skin *in vivo*, limits comparative assessment of the microconduits that are fashioned by insertion of the studied microneedle devices into the two treatment sites.

The channel created by insertion of a hypodermic needle extends into the dermis. Therefore, therapeutics delivered using the traditional Mantoux technique, e.g.

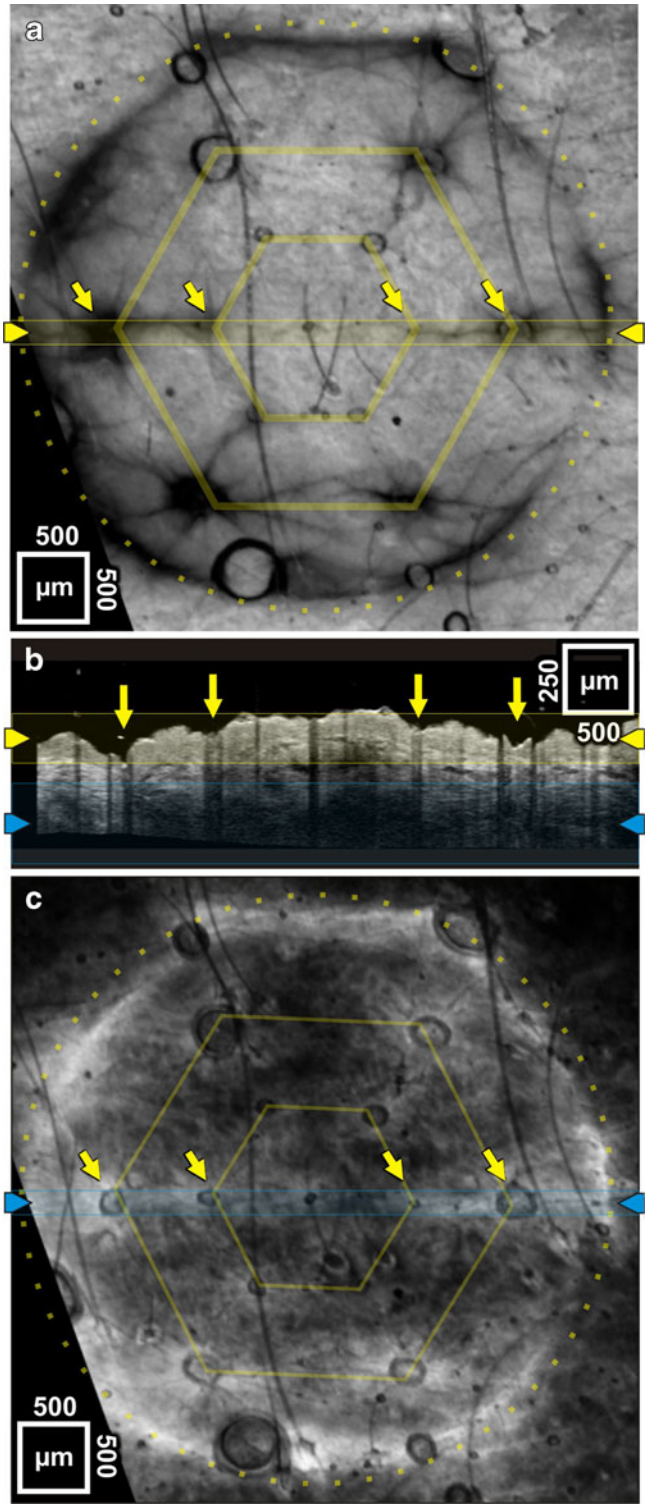

Fig. 13 OCT images of human skin of the upper arm, treated with the polymer microneedle array. The *en face* image in (**a**) is obtained by OCT analysis of the skin tissue at a superficial location within the epidermal layer, as marked by the *yellow* indicator in cross-section (**b**), while the *en face* image in (**c**) is obtained at an underlying location (identified by a *blue* indicator). The *yellow circular dotted line* highlights the impression of the edge of the polymer array, and the hexagonal structures provide a guide to the location of the two rings of microneedles, which would be positioned at vertices. *Yellow arrows* are used to identify microneedle-induced microdisruptions. The latter appear as dark signal-free impressions in the epidermis and as compressed, highly scattering bright regions in the dermis (**c**).

vaccines, would primarily be deposited in this region of the tissue. However, this delivery technique causes pain and bleeding. Conversely, microneedle insertion appeared to create microchannels that were primarily confined to the epidermal layer. In fact, following removal of the silicon and polymer microneedles used in this study, microchannels were almost undetectable, appearing only as minor disruptions to the skin surface. This simple observation, *in vivo*, supports the primary principle of the microneedle device as a minimally invasive means to facilitate delivery of medicaments to the epidermal layer of human skin.

Sub-surface *en face* OCT images are comparable to *en face* images captured in previous studies by identification of skin surface disruptions using a simple dye (25–29). However, lateral diffusion of these dyes can result in over-estimation of the microchannel diameter; therefore, OCT produces a more accurate measurement. Importantly, OCT analysis also provides transverse images of microneedle-treated skin, *in vivo*, without tissue preparation. Prior to this study, the most representative transverse images of microneedle-induced microchannels were obtained by traditional histological analysis of excised skin tissue from patients or cadavers. Removal of the tissue from the biological environment results in significant alterations to the skin, including an inevitable change in the tension of the individual skin layers due to the loss of transversal mechanical stress, the removal of supportive sub-cutaneous layers and altered hydration. Excised human skin is therefore not an accurate representation of the *in vivo* state. Further, subsequent traditional histological processing stages, i.e. fixation, sectioning and histological staining of the skin, cause artefacts related to factors such as dehydration of the tissue and mechanical insult. The results presented in this study therefore provide a more accurate representation of microneedle penetration into human skin.

The skin penetration of an in-plane steel microneedle device has previously been characterised by traditional methods (49). The images of microchannels obtained using conventional methods, however, show a number of differences to OCT images. Most notably, microchannels that are visualised following histological preparation have greater dimensions than equivalent OCT images, i.e. in histological sections, the channels penetrate further and create a markedly wider conduit than OCT images indicate. This is attributable to the tissue-processing factors described previously and, more importantly, the elastic properties of human skin *in vivo*. Application of the array of steel microneedles appears to restrict penetration further, possibly due to the distribution of pressure and a bed-of-nails effect. Smaller microneedles, present on the silicon device, created minor epidermal disruptions in the palmar and upper arm region rather than obvious conduits across the skin barrier (Figs. 11 and 12). Comparison of OCT images with previously published histological images of microchannels created by these silicon devices (22) supports the general principle that histological techniques overestimate the dimensions of microneedle-created microchannels.

This observation has a number of implications. First, microneedle devices are possibly less invasive than previously suggested; therefore, the risk of microbial infection following microneedle treatment is likely to be low (50). This is an important safety issue that is likely to promote the use of microneedles in the clinical setting. Conversely, for the development of two-step delivery systems that use a transdermal patch to deliver medicaments across a microneedle-treated area of skin, i.e. the "poke-with-patch" concept (51), the physical pathway may be more restrictive than previous histological images suggest. Although excised human skin is a crucial laboratory model for examining localised and transdermal delivery of drugs and vaccines (24), it is important to recognise the limitations of an *ex vivo* system. However, greater understanding of the biomechanics of human skin may enable the *in vivo* state to be better reproduced in the laboratory.

Transverse images of in-plane steel microneedles, *in situ* (Fig. 5d), suggest that during microneedle application the entire microprojection does not protrude fully into the skin. Indeed, microneedle penetration does not appear to be reproducible within a single device; the outer microneedle of the in-plane row penetrates to the hilt, whilst adjacent microneedles insert less than half of their needle shaft into the skin. Repeatable differences in the penetration characteristics of microneedles, positioned at different locations within an ordered arrangement, are consistent with previous *en face* observations (26). The transverse images (Fig. 5d) indicate that the skin resists insertion of the device, with deformation of the skin tissue apparent around individual microneedles and compression of the stratum corneum layer observed directly below the needle tip. These *in situ* observations have numerous implications for the microneedle research community and the future clinical use of the microneedle device.

A major proposed therapeutic application of the microneedle device is the minimally invasive, intradermal delivery of vaccines such as influenza. This strategy relies on localised vaccine delivery to the immune responsive viable cells of the epidermis. *In situ* images (Fig. 5e) have confirmed that microneedle devices containing 700-μm projections can successfully penetrate to a depth of approximately 200 μm below the skin surface. In the thick skin of the palmar region, this may only facilitate direct delivery of a medicament to the stratum corneum layer. However, at the upper arm site (an accepted site for intradermal vaccination), this would result in direct access of the vaccine to its target region, the viable epidermis. This highlights the importance of developing microneedle delivery systems that are specific to a treatment site. This was underlined further by the prototype polymer device, which failed to penetrate the thickened stratum corneum of palmar skin but successfully negated the skin barrier in the architecturally distinct upper arm region. Current penetration studies utilise either animal or human skin that has been excised from various anatomical sites, which are often not representative of the proposed therapeutic treatment site, neither in their anatomical thickness nor their elasticity. *In vivo* data, produced by the OCT system, can therefore be used in conjunction with laboratory studies, performed in *ex vivo*/*in vitro* models, to ensure that clinically

effective and safe microneedle delivery systems, including mounts and application procedures, are developed.

Additionally, *in situ* images also provide useful information relating to the potential deposition site for medicaments upon penetration of a coated microneedle delivery system. Coated microneedles provide a means to deliver a number of therapeutics. Dosing, restricted by the coating capacity, is recognised as the limiting factor in this delivery system; therefore, efforts have been made to optimise coating (17,44,52). However, delivery of the coated dose relies upon contact and subsequent rapid dissolution of the coating in the sub-surface aqueous environment of the skin tissue. Images of *in situ* steel microneedles (Fig. 5d) and the microchannels that are subsequently created by this device (Fig. 6c) suggest that only a proportion of the microneedle shaft penetrates into the tissue. Therefore, coating of the entire microneedle shaft with a pre-determined dose of medicament would not result in complete transfer of this dose to the skin tissue and even less into the sub-stratum corneum layers. In order to combat this, coatings could be restricted to the tips of microneedles, and/or devices could be modified to enhance the depth of skin penetration. This would ensure accurate dosing from the microneedle device and would also reduce drug wastage.

Similarly, these factors should also be considered in the development of biodegradable microneedles (10). Degradation of an inserted microneedle, *in situ*, is dependent on dissolution of the needle body within the aqueous tissue environment. Therefore, to determine the delivery characteristics of biodegradable microneedles, it will be important to determine the portion of the microneedle that will degrade following application to the skin tissue. This may influence the design of the microneedle structure and/or loading of the therapeutic, e.g. the titrated dose of the therapeutic may only be loaded into the tip of the microneedle. Alternatively, it may be appropriate to design microneedles using non-biodegradable materials but to include a biodegradable drug-loaded tip. Interestingly, the OCT system would be an effective means of imaging microneedle insertion and also to assess the deposition and subsequent degradation kinetics of the biodegradable portion of the delivery system, *in situ*, due to a difference in the refractive index of the substrate and the skin.

Microneedle technology has made significant advances in the previous decade, and studies have proven the primary concept of the delivery system as a means to painlessly deliver a diversity of therapeutics across the skin barrier. However, there are a number of considerable challenges to address before microneedle devices become a clinically useful tool, including reproducible penetration of human skin, improved methods of drug loading and controlled deposition of therapeutics into a target area within the stratified skin tissue. The studies detailed in this manuscript have provided an early insight into the potential of the OCT system as a powerful research tool for evaluating the microneedle device and other transdermal delivery systems. Importantly, *in vivo*, non-invasive imaging of sub-surface skin architecture can provide the researcher with instant feedback on the performance of devices, and acquisition of highly detailed data-volumes permits detailed analysis of the three-dimensional interaction of the tissue and the delivery system. Future studies may use the OCT system to evaluate the penetration characteristics of a diversity of microneedle designs (various geometries, morphologies and arrangements), device materials and application methods. This screening process would be a significant advance on current imaging techniques, both practically and scientifically, and has the potential to significantly accelerate the optimisation of microneedle devices. Further, OCT imaging could possibly be used in conjunction with the microneedle-based drug delivery system in the clinic to guide microneedle insertion for the delivery of therapeutics to a specific depth at a targeted location in the stratified skin tissue. Finally, following microneedle treatment and subsequent OCT analysis of human skin, the tissue is not sacrificed; therefore, this non-invasive imaging technique also facilitates functional imaging of skin in its natural state, i.e. repeated imaging to examine changes in the tissue over a prolonged period of time.

CONCLUSION

This investigation has utilised a state-of-the-art OCT imaging system, optimized for dermatologic application, to provide the first *in vivo* images of sub-surface human skin layers in response to microneedle insertion. These images provide representative illustrations of microneedle penetration and have also permitted analysis of the epidermal/dermal disruptions that remain following removal of microneedle devices and also a conventional hypodermic needle. Microchannels created in the upper skin layers by microneedles are less invasive than previous histology predicts, and penetration depth was shown to be influenced by multiple parameters, not only microneedle length. In this study, a limited range of locations and subjects were investigated, and further work is required to determine the influence of microneedle structure and human skin biomechanics on the penetration characteristics of a device. Importantly though, this study has successfully utilised the OCT imaging system to provide a non-invasive means of *in vivo* skin characterisation and has demonstrated the potential value of OCT in the future development and optimization of microneedles and other transdermal delivery systems.

ACKNOWLEDGEMENTS

We would like to acknowledge the support of Jessika Weingast from the Division of General Dermatology at the Department of Dermatology of the Medical University of Vienna. This research was supported in part by the BBSRC, Cardiff University, FP6-IST-NMP-2 STREPT (017128, NanoUB), DTI grant (OMICRON), AMR grant (AP1110), European Union project FUN OCT (FP7 HEALTH, contract no. 201880) and CARL ZEISS Meditec Inc.

REFERENCES

1. Bos JD, Meinardi M. The 500 Dalton rule for the skin penetration of chemical compounds and drugs. Exp Dermatol. 2000;9(3):165–9.
2. Badkar AV, Smith AM, Eppstein JA, Banga AK. Transdermal delivery of interferon alpha-2B using microporation and iontophoresis in hairless rats. Pharm Res. 2007;24(7):1389–95.
3. Bramson J, Dayball K, Evelegh C, Wan YH, Page D, Smith A. Enabling topical immunization via microporation: a novel method for pain-free and needle-free delivery of adenovirus-based vaccines. Gene Ther. 2003;10(3):251–60.
4. Birchall J, Coulman S, Anstey A, Gateley C, Sweetland H, Gershonowitz A, *et al.* Cutaneous gene expression of plasmid DNA in excised human skin following delivery via microchannels created by radio frequency ablation. Int J Pharm. 2006;312(1–2):15–23.
5. Levin G, Gershonowitz A, Sacks H, Stern M, Sherman A, Rudaev S, *et al.* Transdermal delivery of human growth hormone through RF-microchannels. Pharm Res. 2005;22(4):550–5.
6. Banga AK. Microporation applications for enhancing drug delivery. Expert Opin Drug Deliv. 2009;6(4):343–54.
7. Gerstel MS, Place VA. Drug Delivery Device. 1976: US.
8. Henry S, McAllister DV, Allen MG, Prausnitz MR. Microfabricated microneedles: a novel approach to transdermal drug delivery. J Pharm Sci. 1998;87(8):922–5.
9. McAllister DV, Wang PM, Davis SP, Park JH, Canatella PJ, Allen MG, *et al.* Microfabricated needles for transdermal delivery of macromolecules and nanoparticles: fabrication methods and transport studies. Proc Nal Acad Sci USA. 2003;100(24):13755–60.
10. Park JH, Allen MG, Prausnitz MR. Biodegradable polymer microneedles: fabrication, mechanics and transdermal drug delivery. J Control Release. 2005;104(1):51–66.
11. Kolli CS, Banga AK. Characterization of solid maltose microneedles and their use for transdermal delivery. Pharm Res. 2008;25(1):104–13.
12. Sivamani RK, Stoeber B, Wu GC, Zhai HB, Liepmann D, Maibach H. Clinical microneedle injection of methyl nicotinate: stratum corneum penetration. Skin Res Technol. 2005;11(2):152–6.
13. Nordquist L, Roxhed N, Griss P, Stemme G. Novel microneedle patches for active insulin delivery are efficient in maintaining glycaemic control: an initial comparison with subcutaneous administration. Pharm Res. 2007;24(7):1381–8.
14. Martanto W, Davis SP, Holiday NR, Wang J, Gill HS, Prausnitz MR. Transdermal delivery of insulin using microneedles *in vivo*. Pharm Res. 2004;21(6):947–52.
15. Li GH, Badkar A, Nema S, Kolli CS, Banga AK. *In vitro* transdermal delivery of therapeutic antibodies using maltose microneedles. Int J Pharm. 2009;368(1–2):109–15.
16. Coulman SA, Barrow D, Anstey A, Gateley C, Morrissey A, Wilke N, *et al.* Minimally invasive cutaneous delivery of macromolecules and plasmid DNA via microneedles. Curr Drug Deliv. 2006;3(1):65–75.
17. Cormier M, Johnson B, Ameri M, Nyam K, Libiran L, Zhang DD, *et al.* Transdermal delivery of desmopressin using a coated microneedle array patch system. J Control Release. 2004;97(3):503–11.
18. Alarcon JB, Hartley AW, Harvey NG, Mikszta JA. Preclinical evaluation of microneedle technology for intradermal delivery of influenza vaccines. Clin Vaccine Immunol. 2007;14(4):375–81.
19. Mikszta JA, Dekker JP, Harvey NG, Dean CH, Brittingham JM, Huang J, *et al.* Microneedle-based intradermal delivery of the anthrax recombinant protective antigen vaccine. Infect Immun. 2006;74(12):6806–10.
20. Widera G, Johnson J, Kim L, Libiran L, Nyam K, Daddona PE, *et al.* Effect of delivery parameters on immunization to ovalbumin following intracutaneous administration by a coated microneedle array patch system. Vaccine. 2006;24(10):1653–64.
21. Coulman SA, Anstey A, Gateley C, Morrissey A, McLoughlin P, Allender C, *et al.* Microneedle mediated delivery of nanoparticles into human skin. Int J Pharm. 2009;366(1–2):190–200.
22. Birchall J, Coulman S, Pearton M, Allender C, Brain K, Anstey A, *et al.* Cutaneous DNA delivery and gene expression in *ex vivo* human skin explants via wet-etch microfabricated microneedles. J Drug Target. 2005;13(7):415–21.
23. Godin B, Touitou E. Transdermal skin delivery: predictions for humans from *in vivo*, *ex vivo* and animal models. Adv Drug Deliv Rev. 2007;59(11):1152–61.
24. Ng KW, Pearton M, Coulman S, Anstey A, Gateley C, Morrissey A, *et al.* Development of an *ex vivo* human skin model for intradermal vaccination: tissue viability and Langerhans cell behaviour. Vaccine. 2009;27(43):5948–55.
25. Bal SM, Caussin J, Pavel S, Bouwstra JA. *In vivo* assessment of safety of microneedle arrays in human skin. Eur J Pharm Sci. 2008;35(3):193–202.
26. Haq MI, Smith E, John DN, Kalavala M, Edwards C, Anstey A, *et al.* Clinical administration of microneedles: skin puncture, pain and sensation. Biomed Microdevices. 2009;11(1):35–47.
27. Sivamani RK, Stoeber B, Liepmann D, Maibach HI. Microneedle penetration and injection past the stratum corneum in humans. J Dermatol Treat. 2009;20(3):156–9.
28. Van Damme P, Oosterhuis-Kafeja F, Van der Wielen M, Almagor Y, Sharon O, Levin Y. Safety and efficacy of a novel microneedle device for dose sparing intradermal influenza vaccination in healthy adults. Vaccine. 2009;27(3):454–9.
29. Gill HS, Denson DD, Burris BA, Prausnitz MR. Effect of microneedle design on pain in human volunteers. Clin J Pain. 2008;24(7):585–94.
30. Levin J, Maibach H. The correlation between transepidermal water loss and percutaneous absorption: an overview. J Control Release. 2005;103(2):291–9.
31. Welzel J. Optical coherence tomography in dermatology: a review. Skin Res Technol. 2001;7(1):1–9.
32. Huang D, Swanson E, Lin C, Schuman J, Stinson W, Chang W, *et al.* Optical coherence tomography. Science. 1991;254(5035):1178–81.
33. Gambichler T, Boms S, Stucker M, Kreuter A, Moussa G, Sand M, *et al.* Epidermal thickness assessed by optical coherence tomography and routine histology: preliminary results of method comparison. J Eur Acad Dermatol. 2006;20(7):791–5.
34. Gambichler T, Matip R, Moussa G, Altmeyer P, Hoffmann K. *In vivo* data of epidermal thickness evaluated by optical coherence tomography: effects of age, gender, skin type, and anatomic site. J Dermatol Sci. 2006;44(3):145–52.

35. Konig K, Speicher M, Buckle R, Reckfort J, McKenzie G, Welzel J, *et al.* Clinical optical coherence tomography combined with multiphoton tomography of patients with skin diseases. J Biophotonics. 2009;2(6–7):389–97.
36. Mogensen M, Nurnberg BM, Forman JL, Thomsen JB, Thrane L, Jemec GBE. *In vivo* thickness measurement of basal cell carcinoma and actinic keratosis with optical coherence tomography and 20-MHz ultrasound. Br J Dermatol. 2009;160(5):1026–33.
37. Neerken S, Lucassen GW, Bisschop MA, Lenderink E, Nuijs TAM. Characterization of age-related effects in human skin: a comparative study that applies confocal laser scanning microscopy and optical coherence tomography. J Biomed Opt. 2004;9(2):274–81.
38. Querleux B, Baldeweck T, Diridollou S, de Rigal J, Huguet E, Leroy F, *et al.* Skin from various ethnic origins and aging: an *in vivo* cross-sectional multimodality imaging study. Skin Res Technol. 2009;15(3):306–13.
39. Welzel J, Reinhardt C, Lankenau E, Winter C, Wolff HH. Changes in function and morphology of normal human skin: evaluation using optical coherence tomography. Br J Dermatol. 2004;150(2):220–5.
40. Alex A, Považay B, Hofer B, Popov S, Glittenberg C, Binder S, Drexler W. Multispectral *in vivo* three-dimensional optical coherence tomography of human skin. J Biomed Opt. 2010;026025.
41. Kim CS, Wilder-Smith P, Ahn YC, Liaw LHL, Chen ZP, Kwon YJ. Enhanced detection of early-stage oral cancer *in vivo* by optical coherence tomography using multimodal delivery of gold nanoparticles. J Biomed Opt. 2009;14(3):034008.
42. Yoon J, Son T, Choi EH, Choi B, Nelson JS, Jung B. Enhancement of optical skin clearing efficacy using a microneedle roller. J Biomed Opt. 2008;13(2):021103.
43. Stumpp O, Welch AJ, Gill HS, Prausnitz MR. OCT analysis of microneedle and Er: YAG surface ablation for enhanced transdermal delivery of hyper-osmotic agents for optical skin clearing. Laser Interaction with Tissue and Cells Xv. 2004;5319:121–9.
44. Gill HS, Prausnitz MR. Coated microneedles for transdermal delivery. J Control Release. 2007;117(2):227–37.
45. Wilke N, Morrissey A. Silicon microneedle formation using modified mask designs based on convex corner undercut. J Micromech Microeng. 2007;17(2):238–44.
46. Unterhuber A, Považay B, Hermann B, Sattmann H, Drexler W, Yakovlev V, *et al.* Compact, low-cost Ti: Al2O3 laser for *in vivo* ultrahigh-resolution optical coherence tomography. Opt Lett. 2003;28(11):905–7.
47. Kim Y-C, Quan F-S, Yoo D-G, Compans RW, Kang S-M, Prausnitz MR. Improved influenza vaccination in the skin using vaccine coated microneedles. Vaccine. 2009;27(49):6932–8.
48. Laurent A, Mistretta F, Bottigioli D, Dahel K, Goujon C, Nicolas JF, *et al.* Echographic measurement of skin thickness in adults by high frequency ultrasound to assess the appropriate microneedle length for intradermal delivery of vaccines. Vaccine. 2007;25(34):6423–30.
49. Kim Y-C, Quan F-S, Compans RW, Kang S-M, Prausnitz MR. Formulation and coating of microneedles with inactivated influenza virus to improve vaccine stability and immunogenicity. J Control Release. 2010;142(2):187–95.
50. Donnelly RF, Singh TRR, Tunney MM, Morrow DIJ, McCarron PA, O'Mahony C, *et al.* Microneedle arrays allow lower microbial penetration than hypodermic needles *in vitro*. Pharm Res. 2009;26(11):2513–22.
51. Prausnitz MR. Microneedles for transdermal drug delivery. Adv Drug Del Rev. 2004;56(5):581–7.
52. Gill HS, Prausnitz MR. Coating formulations for microneedles. Pharm Res. 2007;24(7):1369–80.